

Summer fireworks on comet 67P

J.-B. Vincent,^{1★} M. F. A’Hearn,² Z.-Y. Lin,³ M. R. El-Maarry,⁴ M. Pajola,^{5,6}
H. Sierks,¹ C. Barbieri,⁷ P. L. Lamy,⁸ R. Rodrigo,^{9,10} D. Koschny,¹¹ H. Rickman,^{12,13}
H. U. Keller,¹⁴ J. Agarwal,¹ M. A. Barucci,¹⁵ J.-L. Bertaux,¹⁶ I. Bertini,⁶ S. Besse,¹⁷
D. Bodewits,² G. Cremonese,¹⁸ V. Da Deppo,¹⁹ B. Davidsson,²⁰ S. Debei,²¹
M. De Cecco,²² J. Deller,¹ S. Fornasier,¹⁵ M. Fulle,²³ A. Gicquel,¹ O. Groussin,⁸
P. J. Gutiérrez,²⁴ P. Gutiérrez-Marquez,¹ C. Güttler,¹ S. Höfner,^{1,14} M. Hofmann,¹
S. F. Hviid,²⁵ W.-H. Ip,^{3,26} L. Jorda,⁸ J. Knollenberg,²⁵ G. Kovacs,^{1,27} J.-R. Kramm,¹
E. Kührt,²⁵ M. Küppers,¹⁷ L. M. Lara,²⁴ M. Lazzarin,⁷ J. J. Lopez Moreno,²⁴
F. Marzari,⁷ M. Massironi,²⁸ S. Mottola,²⁵ G. Naletto,^{29,19,6} N. Ockay,¹ F. Preusker,²⁵
F. Scholten,²⁵ X. Shi,¹ N. Thomas,⁴ I. Toth^{8,30} and C. Tubiana¹

Affiliations are listed at the end of the paper

Accepted 2016 September 21. Received 2016 August 26; in original form 2016 June 17

ABSTRACT

During its 2 yr mission around comet 67P/Churyumov–Gerasimenko, ESA’s *Rosetta* spacecraft had the unique opportunity to follow closely a comet in the most active part of its orbit. Many studies have presented the typical features associated with the activity of the nucleus, such as localized dust and gas jets. Here, we report on series of more energetic transient events observed during the 3 months surrounding the comet’s perihelion passage in 2015 August. We detected and characterized 34 outbursts with the *Rosetta* cameras, one every 2.4 nucleus rotations. We identified three main dust plume morphologies associated with these events: a narrow jet, a broad fan, and more complex plumes featuring both previous types together. These plumes are comparable in scale and temporal variation to what has been observed on other comets. We present a map of the outbursts’ source locations, and discuss the associated topography. We find that the spatial distribution sources on the nucleus correlate well with morphological region boundaries, especially in areas marked by steep scarps or cliffs. Outbursts occur either in the early morning or shortly after the local noon, indicating two potential processes: morning outbursts may be triggered by thermal stresses linked to the rapid change of temperature; afternoon events are most likely related to the diurnal or seasonal heat wave reaching volatiles buried under the first surface layer. In addition, we propose that some events can be the result of a completely different mechanism, in which most of the dust is released upon the collapse of a cliff.

Key words: comets: individual: 67P/Churyumov–Gerasimenko.

1 INTRODUCTION

The Optical, Spectroscopic, and Infrared Remote Imaging System (OSIRIS) cameras on board ESA’s *Rosetta* spacecraft have monitored the activity of comet 67P-Churyumov–Gerasimenko (67P) across varying heliocentric distances (4–1.24 au) and different seasons on the nucleus (subsolar latitude between +45° and –55°). Previous publications focused particularly on coma features

usually referred to as jets: collimated streams of dust and gas arising from the nucleus. The foot prints of these features on 67P, their migration with the seasons and heliocentric distance, their relation to topography, their photometry, and possible formation mechanisms are described in details in Lara (2015), Lin (2015), Lin et al. (2016) and Vincent et al. (2016).

One of the striking discoveries of *Rosetta* has been the clockwork repeatability of jets from one rotation to the next. Jets are very dynamic by nature, depending on the complex hydrodynamics of the gas and dust streams interacting with the local topography, and controlled by local thermal conditions. They grow and fade with

* E-mail: vincent@mps.mpg.de

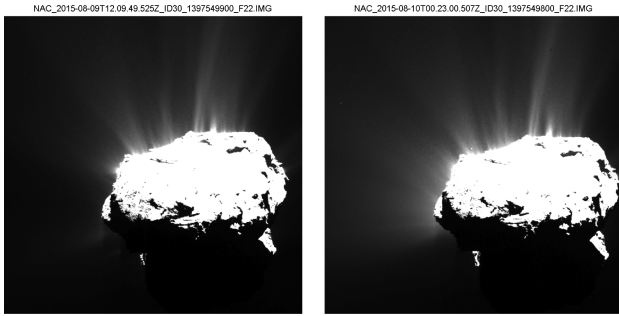


Figure 1. Example of two images acquired on 2015-08-09T12.09.49 (left) and 2015-08-10T00.23.00 (right), almost one rotation apart (rotation period – images separation = 5^m33^s). Both image contrasts are stretched to the same level (5 per cent of the same maximum brightness value). Field of view $1^\circ \times 1^\circ$, distance = 305 km, and resolution = 5.7 m px^{-1} .

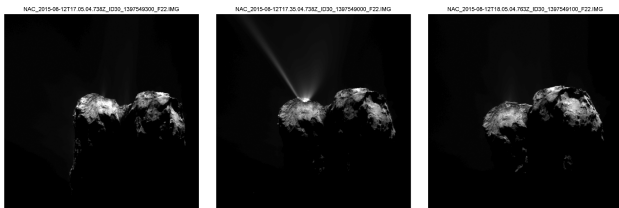


Figure 2. A transient event detected on the day of perihelion (2015 August 12). Images are separated by only 1/2 h, contrast but not enhanced. Observations before and after the event show only faint activity from the outbursting area, while the image at 17:35 reveals a plume of material as bright as the nucleus, expanding at least 10 km from the source. Field of view $1^\circ \times 1^\circ$ degree, distance = 332 km, resolution = 6.1 m px^{-1} . Outburst #14 is in Table 1.

the solar illumination as the nucleus rotates, but the same exact features can be observed from one rotation to the next. Fig. 1 shows an example of this phenomenon. This, of course, puts constraints on the thermophysics and volatile content of active areas, which needs to ensure the sustainability and repeatability of the jets we observed.

Long-lasting repetitive features are however not the only manifestation of activity on comet 67P. In this paper, we report on another types of events, much more transient in nature, which were observed most frequently around the summer months of 67P’s Southern hemisphere, i.e. from 2015 July to September, when the comet reached its perihelion (2015 August 13, 1.24 au).

These events are characterized by the sudden and short release of a dust, sometimes collimated but not necessarily. While the typical jets are relatively faint (about 10 per cent of the nucleus surface brightness), the plumes ejected by these outbursts are usually as bright as the nucleus, and they can be detected in our images without enhancing the contrast. Contrary to the jets that last for several hours, most transient events are observed only once, indicating a lifetime shorter than the cadence of our images (between 5 and 30 min, depending on the observing sequence). One sequence showing a transient event is presented in Fig. 2.

We report here our detection of these transient events, during a 3-month period surrounding the perihelion passage. In the following text, transient events will alternatively be referred to as *outbursts* to indicate their sudden and bright behaviour, bearing in mind that they are many orders of magnitude fainter than typical cometary outbursts detected routinely by ground-based observers for other comets.

2 DATA AND METHODS

2.1 Detection

We used monitoring data acquired by the OSIRIS Narrow Angle Camera (NAC) and Wide Angle Camera (WAC), as well as *Rosetta*’s navigation camera (NavCam) to increase our temporal coverage. Around perihelion, OSIRIS monitoring campaigns were run on a weekly basis, with a set of images acquired every 1/2 h for slightly longer than the current nucleus rotation period ($12^h18^m10^s$ at perihelion). After noticing the first outbursts in 2015 July, we increased the cadence of images in each observation, and reduced the time between monitoring campaigns to a few days. In addition to the OSIRIS data, we also looked for transient events in the navigation images, acquired about every 4 h during the whole mission.

To distinguish between outbursts and other short-lived features, we established the following definition: an outburst is identified by a sudden brightness increase in the coma, associated with the release of gas and dust over a duration very short with respect to the rotation period of the nucleus. Outbursts plume are typically detected in one image only, depending on the observing cadence. The dust plume is typically one order of magnitude brighter than the usual jets. We did not impose plume morphology as a criterion.

Following this definition we identified 34 events in our data set, listed in Table 1. Among them, 26 were detected with OSIRIS NAC, 3 by OSIRIS WAC, and 5 by the NavCam. A visual catalogue of the brightest events is provided in Fig. 3. A timeline of these detections is given in Table 1 and Fig. 5.

2.2 Source location

We estimated the source location of each event with the following three techniques.

In most cases (for instance Fig. 2), the ejected dust plume arises from one area in the field of view of our cameras. We measure directly the 2D coordinates of the source pixel in the image, and project this position in three dimensions on the most accurate shape model of 67P, obtained from stereo-photogrammetry for the Northern hemisphere (Preusker et al. 2015) and stereo-photoclinometry for the Southern hemisphere (Jorda et al. 2016). The projection from image to shape is done using the spacecraft and comet reconstructed attitudes and trajectories provided by the SPICE library (Acton 1996). We verify this position by producing synthetic images from the orbital parameters and camera descriptions, and matching the synthetic view with the original image. The largest uncertainty on this type of source inversion comes from the resolution of the images ($3\text{--}6 \text{ m px}^{-1}$ for the NAC, $15\text{--}32 \text{ 40 m px}^{-1}$ for the WAC, and $15\text{--}83 \text{ m px}^{-1}$ for the NavCam). This is the typical error for most of our observations.

If the source is not visible (typically just behind the horizon) but the plume is detected more than once (i.e. when acquiring multi-spectral images), we use the slightly different viewing geometry between the images to triangulate the source position. This technique is commonly used to find jet sources and is described in detail in Vincent et al. (2016). This leads to a maximum error smaller than 300 m on the surface, along the line-of-sight direction.

Finally, if the source is not visible and the plume is seen only in one image, then we can only roughly infer the source location. We noticed however that dust plumes released during outburst events are often brighter than the nucleus very close to the source. We used this to constrain how far the source must lie beyond the horizon,

Table 1. Detected outbursts and locations of their sources.

Id	Date (UTC)	Camera	hdist (au)	cdist (km)	Lat (°)	Lon (°)	Sun lat (°)	Sun lon (°)	Relative luminosity (%)	Type	Time since sunrise (h)
01	2015-07-10T02:10:18	NavCam	1.311	155.16	74	200	-30.51	131.65	0.00	B	3.62
02	2015-07-19T03:38:09	NAC	1.281	180.00	-24	296	-35.70	292.44	2.43	A	3.09
03	2015-07-26T20:22:42	NAC	1.261	168.00	-36	75	-39.94	316.99	7.07	B	11.16
04	2015-07-27T00:14:29	NAC	1.261	168.00	-31	333	-40.03	204.51	1.94	A	10.24
05	2015-07-28T05:23:43	WAC	1.259	180.87	-4	264	-40.67	75.48	0.51	B	10.73
06	2015-07-29T13:25:28	NAC	1.256	186.00	-37	300	-41.37	222.65	15.58	A	3.69
07	2015-08-01T10:53:15	NAC	1.252	214.05	-12	196	-42.84	358.46	1.41	B	10.51
08	2015-08-01T15:44:50	NAC	1.251	211.00	-28	34	-42.94	216.81	11.71	B	10.68
09	2015-08-03T17:27:03	WAC	1.249	218.49	-75	303	-43.94	207.71	0.55	B	9.97
10	2015-08-05T07:25:05	NAC	1.247	253.00	-25	320	-44.69	180.67	1.90	A	10.32
11	2015-08-05T08:05:15	NAC	1.247	253.00	-23	318	-44.70	161.14	1.90	A	10.47
12	2015-08-08T15:21:48	NavCam	1.244	303.00	-30	51	-46.17	7.96	0.00	C	3.41
13	2015-08-09T09:15:14	NAC	1.244	304.00	-30	298	-46.48	205.71	3.05	A	9.94
14	2015-08-12T17:21:20	NAC	1.243	332.00	-30	58	-47.81	26.46	100.00	C	3.32
15	2015-08-21T09:44:53	NavCam	1.247	330.00	-32	227	-50.54	52.98	0.00	B	10.61
16	2015-08-22T06:47:04	NavCam	1.248	336.00	-40	168	-50.75	157.23	0.00	C	3.15
17	2015-08-22T23:46:21	WAC	1.249	334.00	-25	316	-50.91	19.88	0.29	B	11.60
18	2015-08-23T01:39:38	NAC	1.249	334.35	-53	292	-50.93	324.60	12.53	A	3.33
19	2015-08-23T15:12:48	NAC	1.251	340.17	-23	314	-51.05	287.77	5.46	A	3.28
20	2015-08-26T07:51:04	NAC	1.254	417.00	-41	42	-51.55	194.51	5.57	B	10.43
21	2015-08-27T22:58:04	NAC	1.257	403.55	-8	321	-51.80	128.16	2.71	B	10.76
22	2015-08-28T02:29:21	NAC	1.257	403.8	-21	24	-51.82	24.94	29.04	C	3.07
23	2015-08-28T10:10:57	NAC	1.258	410.29	-31	229	-51.86	159.42	69.84	B	3.63
24	2015-09-05T08:50:02	NAC	1.276	436.07	-15	26	-52.31	325.22	27.89	C	11.63
25	2015-09-05T09:00:02	NAC	1.276	435.4	-31	330	-52.31	320.33	66.73	C	3.14
26	2015-09-10T08:59:49	NAC	1.291	317.9	-25	67	-52.04	33.74	1.83	C	3.33
27	2015-09-10T13:06:14	NAC	1.292	317.41	-23	292	-52.03	272.97	6.47	A	3.22
28	2015-09-10T13:36:14	NAC	1.292	317.38	-21	307	-52.02	258.27	9.44	C	3.46
29	2015-09-10T14:11:15	NAC	1.292	317.34	-15	10	-52.02	241.10	7.97	B	11.07
30	2015-09-10T18:57:41	NAC	1.292	317.54	-15	10	-52.00	100.71	4.37	A	9.93
31	2015-09-10T19:27:41	NAC	1.292	317.6	-30	286	-52.00	86.00	7.45	C	10.82
32	2015-09-12T09:41:00	NAC	1.298	329.89	-12	318	-51.82	41.69	15.96	C	11.44
33	2015-09-14T18:47:00	NAC	1.306	316.29	-25	198	-51.49	161.29	35.21	C	3.36
34	2015-09-26T12:03:32	NavCam	1.356	817.64	-40	307	-48.86	149.76	0.00	A	10.47

Column description: identification number of the outburst, date, camera which detected the event, 67P heliocentric distance, *Rosetta* cometocentric distance, latitude and longitude of the source, latitude and longitude of the subsolar point, relative intensity with respect to the brightest event, type of outburst. Time since sunrise is an estimation of the local time on the surface (see Section 3.4; based on a 12.25 h rotation period, a time since sunrise = 3 h indicates the local mid-day, while a time since sunrise = 12 h is the end of the night/early morning).

and found a maximum uncertainty of about 10° in latitude and longitude, equivalent to about 300 m on the surface.

Sources with large uncertainties (9 out of 34) are indicated with an error ellipse on the map given in Fig. 6. All other positions have an uncertainty comparable to the size of the symbol used to mark the source location on the figure.

2.3 Relative intensity of outbursts

Characterizing the ejected mass per outburst is challenging because of its transient nature. As we see the event in one image only during a given sequence, we can only know that all the material was ejected in the time frame covered by three images, as in Fig. 2. We do not know if the image showing the dust plume was acquired shortly after the outburst started, or later in the process. Additionally, the plume often extends beyond our field of view and we do not know enough about the acceleration regime to be able to extrapolate the visible brightness profile. However, when we had the chance to follow an outburst for more than one image (i.e. outburst #26), we saw that the total duration of the event was at most a couple of minutes. This means any image showing an outburst is likely to have been

acquired very shortly after the event started, and therefore most of the ejected material is still in the field of view. For the same reason, outbursts are likely to have been observed in a similar stage of development and by integrating their brightness over a large area we can ignore local variations due to the non-steady state of the plume.

For each event, we integrated the total radiance ($\text{W m}^{-2} \text{sr}^{-1} \text{nm}^{-1}$) measured in a trapezoid box extending along the edges of the plume from a distance of 50 to 500 m. The closest boundary was chosen to avoid capturing any remnant signal from the illuminated nucleus, in case the ejected dust cloud is not optically thick. The furthest boundary is arbitrarily set 10 times further to ensure that we capture enough material to draw a meaningful comparison, independently of the plume morphology. This means we typically integrated about 5000 NAC pixels per outburst. The integrated radiance is converted to luminosity (Wnm^{-1}) by a multiplication with the factor $4\pi\text{cdist}^2$, with *cdist* being the distance between *Rosetta* and the comet. This luminosity is finally normalized to the brightest outburst we observed in this period (#14: 12 2015 August, a.k.a. ‘perihelion outburst’). The luminosity of this event, integrated in the window described above,

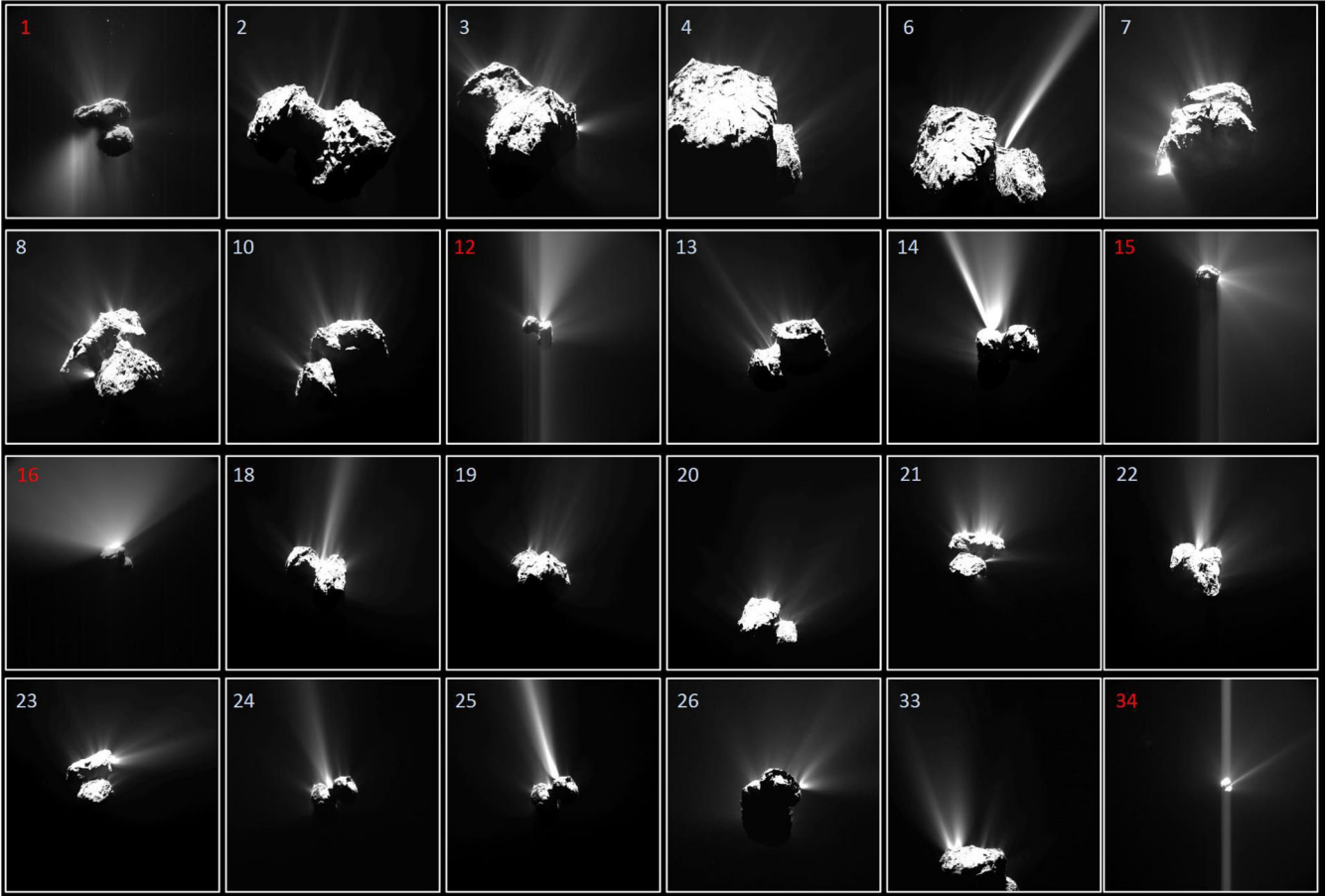


Figure 3. Mosaic of the brightest OSIRIS NAC (white) and NavCam (red) outbursts detected by *Rosetta* from 2015 July to September. Observation details are given in Table 1; see acknowledgments for detailed credit lines of the images.

was measured to be 1.18×10^{13} W at 649.2 nm (OSIRIS NAC Orange filter ‘F22’).

The perihelion outburst was the strongest ever observed, at least an order of magnitude above most of the other events. A more average outburst was observed on July 29 (#06 in Table 1). By chance, most *Rosetta* instruments were acquiring data at that time and the first results of this common analysis have been presented online shortly after the event (<http://blogs.esa.int/rosetta/2015/08/11/comets-firework-display-ahead-of-perihelion>). We modelled the photometric profile of the July 29 event using the approach described in Knollenberg (2016). In short, we convert the radiance over an image area as described above, convert it to a dust cross-section, and then to mass assuming a dust size distribution with a power law of -2.6 . For this specific event, we estimated an ejected flux of $60\text{--}260$ kg s $^{-1}$ for particles in the range of $1\text{--}10$ μm or $1\text{--}50$ μm . This is equivalent to $4\text{--}17$ per cent of the total dust flux being ejected by the comet with its nominal activity at perihelion (1500 kg s $^{-1}$; Fulle et al. 2016). We know from other events and the cadence of our images that outbursts last less than 5 min. Therefore, the maximum mass of dust ejected by this event is of the order of $20\text{--}80$ tons.

This mass loss per outburst is comparable to what has been observed on, at least, another comet. We have estimated the mass ejected in the outburst by 9P/Tempel 1 on 2005 Jul 2 (A’Hearn et al. 2005) using the archived photometry from Deep Impact (Bastien et al. 2008; Deep Impact MRI Photometry of Comet 9P/Tempel

1 V1.0, DIF-C-MRI-5-TEMPEL1-PHOTOMETRY-V1.0, NASA Planetary Data System) and common assumptions about the relationship between brightness and dust. This outburst was $2/3$ the brightness of the ambient coma at all radii and the total mass was 300 tons ejected over 10 min, therefore an outburst flux of 500 kg s $^{-1}$, of the same order as the values we have found for 67P.

At the time of writing this paper, the NavCam data are not calibrated. We indicate these events in our timeline but arbitrarily set their relative brightness to zero. Some did however saturate the NavCam CCD when the nucleus did not (i.e. outburst #15, on 2016 Aug 21), so one can expect that after calibration they will appear at least as strong as the outbursts typically detected by OSIRIS.

3 RESULTS

3.1 Morphological classification of the dust plumes

We distinguish at least three types of dust plumes morphology associated with outbursts, from which we derived the following classification.

- (i) Type A: they produce a much collimated jet which expands beyond our field of view (typically 10 km). They extend further away from the nucleus than the other types.
- (ii) Type B: broad plumes, or wide dust fans. They expand much more laterally than radially when compared to type A plumes.

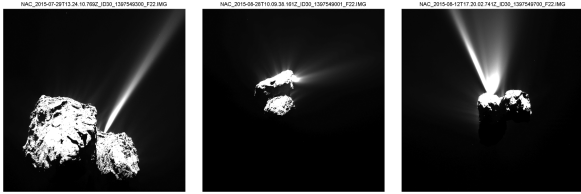


Figure 4. The three major morphologies of outbursts defined as types A (jet), B (broad plume), and C (complex) in Section 3.1. Outbursts #06, #23, and #14 in Table 1.

(iii) Type C: complex events, often combining both a narrow and a broad feature. To the best of our knowledge both features arise from the same source, within the error ellipse of our detection.

All morphologies seem equally probable. The type of each event is indicated in Table 1 and an example of each is given in Fig. 4. It is important to stress that this classification is purely morphological. It is not clear whether the three types correspond to different mechanisms or if they are different stages of a same process.

We can constrain the dust velocity in these plumes by using the cadence of our images. For instance, the plume associated with event #25 extends by at least 8150 m (edge of the NAC frame) and was not detected in the previous image acquired 10 min earlier. This implies that dust was ejected with a minimum velocity of 13 ms^{-1} . This is at least one order of magnitude larger than the typical velocity of dust grains in 67P’s jets (1 ms^{-1} ; Lin et al. 2016), indicative of more energetic events.

We tried to identify whether the different plume morphology reflects an evolutionary process in the outburst mechanism. We looked for morphological variations when the imaging cadence showed the same event in several images but could not observe any change of morphological type, only the expansion of the dust plume. None the less, we cannot exclude an observational bias.

If there is indeed an evolution, it seems that the most reasonable sequence would be type A > type C > type B.

(i) The event starts with some dust and gas being ejected at high velocity in a narrow plume (type A). This is indicative of a small source area, possibly confined.

(ii) As the outbursts unravels, the local surface is modified (collapse or ‘eruption’) and exposes a larger fraction of fresh material leading to the formation of a broader plume (type C).

(iii) Finally, the morphology of the source area has changed enough to not be able to collimate the initial narrow flow anymore, and only the broad plume survives (type B).

3.2 Timeline of detected outbursts

The summer outbursts presented here are not the first ones detected by the OSIRIS cameras on comet 67P. We did observe a large outburst in 2014 April, at a distance of 4 au (Tubiana 2015). We did not detect any further event as *Rosetta* was closing in to the comet, down to a distance of 10 km in 2014 October. As the OSIRIS cameras were mapping the nucleus with high cadence imaging from 2014 July to October, it is unlikely that we have missed an outburst in this period. The next event occurred in 2015 February at a distance of 2.5 au and is described in Knollenberg (2016). Although much smaller in scale than most of the other events, it is particularly interesting because it arose from an area that had been in the night for 5 h when the outbursts occurred.

We did not detect any other event between 2015 February and the first summer event in 2015 July. It is however possible that we missed some, as the high dust content in the vicinity of the spacecraft triggered safing events and a retreat to several hundred kilometres from the nucleus, which prevented us from monitoring the activity as usual. Other instruments may have detected a few events in this time frame.

The OSIRIS cameras acquired 11 807 images from 2015 July 1 to September 30, with an average time separation of 12 min. Among these observations, we ran 12 dedicated outburst campaigns aimed at detecting and characterizing transient events with fast cadence imaging: one observation every 5 min, for a few hours. Fig. 5 shows the timeline of our detections. We observed 34 events, about one every 1.27 d, i.e. every 2.37 comet rotations (period = 12.25 h).

Comparing the timeline of detected transient events with the cadence of our images gives us a hint of the completeness of our catalogue. For instance, one can see that we may have missed several events in the first half of 2015 July due to poor time coverage. The same is true for the last week of 2015 September during which we did not observe for 24 consecutive hours. However, the rest of the timeline is densely covered with observations, and the gaps in outburst detection cannot be explained by lack of imaging. This is particularly true for the first half of 2015 August or the week around 2015 September 10 during which we did not detect any event in spite of continuous high-cadence monitoring. In addition to that, it happened several times that we observed the comet in consecutive rotations for 1 or 2 d during which only one event was detected. For instance, the full set of observations acquired around perihelion from August 9 to 13 yielded only two events (August 9 and 12).

Therefore, it seems likely that the cadence of one outburst every 2.4 comet rotations is close to the real cadence of such events, and it may have implications on the related mechanism (see Section 4). This cadence is comparable to what has been reported for comet 9P/Tempel 1:1 outburst every 3.3 d, i.e. every second comet rotation (period = 40 h).

Note that we consider here only events producing a dust feature detectable without enhancing the contrast of our images, i.e. comparable in brightness to the nucleus. We also see short-lived jets in almost every sequence, and their number of detection increases with the imaging cadence. They are however very faint, typically less than 10 per cent of the nucleus brightness. Apart from their short duration, they behave comparably to all other nominal jet features.

3.3 Source locations and local morphology

3.3.1 Global map

Fig. 6 shows all outburst sources projected on a topographic map of 67P, and on a morphological map displaying the regions boundaries. All but one sources are located in the Southern hemisphere, between 0° and -50° of latitude, i.e. around the subsolar latitude for this period (it varied from -30° to -55°). This is consistent with previous observations showing that active sources, in general, migrate with the Sun (Vincent et al. 2016; Ip 2016). Outburst sources are not evenly distributed along this latitude. We observe some clustering in three main areas: (1) the Anhur–Aker boundary (big lobe), (2) the Anuket–Sobek boundary (big lobe), and (3) the Wosret–Mafet boundary (small lobe). These areas are characterized by steep scarps, cliffs, and pits, which contrast with the overall flatter morphology of the Southern hemisphere. It is interesting to note that beyond these three areas, it seems like all outbursts sources

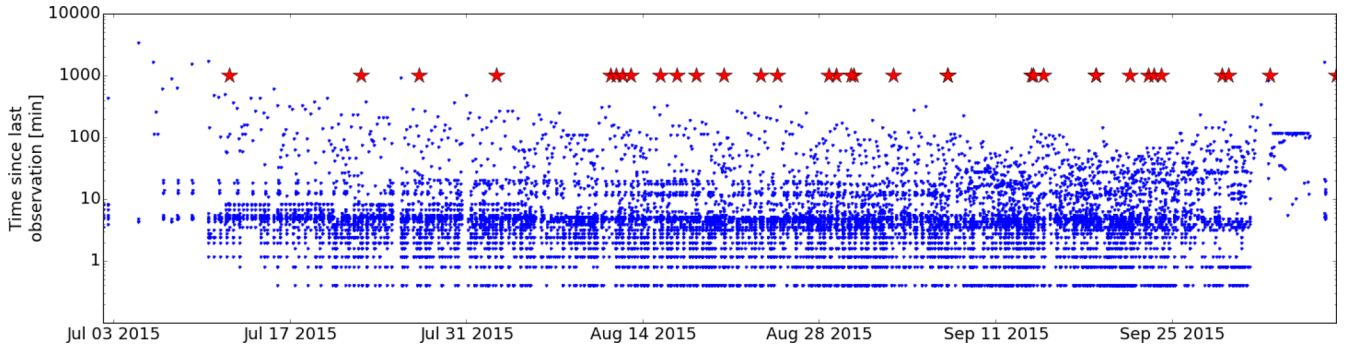


Figure 5. Timeline of images and outbursts detection over the summer 2015. Every blue dot represents an image acquisition, with the vertical axis showing how much time passed since the last observation. Red stars represent outburst detections.

are located close to morphological boundaries, i.e. areas where we observe discontinuities in the local terrain, either textural or topographic. Region boundaries are defined in El-Maarry et al. (2015b, 2016). This seems to indicate a link between morphology and outbursts, although it is not clear which one influences the other. We will discuss this further in Section 4.

3.3.2 Local morphology

The local morphology, especially at the time of the outburst, is more difficult to characterize for several reasons. All the events reported here were observed around perihelion while *Rosetta* was orbiting ~ 300 km from the nucleus. This distance corresponds to a spatial resolution of ~ 6 m px^{-1} , with the OSRIS NAC. Following perihelion passage, *Rosetta* undertook an excursion into the plasma tail at 1500 km away before approaching back slowly to the nucleus. As a result, high-resolution images (< 1 m px^{-1}) could only be acquired from 2016 February onwards, when *Rosetta* went back to distances lower than 50 km. Additionally, the illumination conditions pre-perihelion were poor for the Southern hemisphere and prevented high-resolution imaging. Therefore, for most of the outbursts only an ‘after’ image acquired 6 months after the event is available. When present, pre-perihelion images have too low spatial resolution for a confident quantitative comparison. Nevertheless, high-resolution images of some of the source regions display interesting morphologies that is of worth mentioning.

Fig. 7 shows a number of outburst spots particularly in the Wosret and Anhur regions as well as notable regional boundaries such as those of Anuket/Sobek and Aker/Anhur. We observe that most sources fall on steep topographic structures such as scarps and pits, often displaying nearby talus deposits. The Wosret region (Fig. 7a) shows two distinctive morphological terrains one where many candidate outburst locations are observed in the pitted terrains as opposed to the heavily fractured and quasi-flat terrains. A link between outbursts and pitted terrains has been explored in detail by Belton et al. (2008) in their review of similar events of comet 9P, although the scale and distribution of pitted terrains are not the same as on 67P. Given the lower resolution of the images of 9P’s surface (at best 10 m px^{-1}), it is not clear whether the outbursts carved out the pits, or if outbursts originate from a subsequent evolution, such as the collapse of the pit walls.

A number of outbursts appear to coincide remarkably with the boundary between Anuket and Sobek (the southern neck, Fig. 7b), and a number of terraces that also show considerable talus deposits. A closer look at the main cliffs of the southern part of the large

lobe shows that many outburst locations appear to coincide either with some of the numerous niches and alcoves in the Anhur region (Fig. 7c). The Anhur region appears to be the most weakly consolidated region in the Southern hemisphere as evident from its morphology, low slope in comparison to other cliff regions, and abundant boulders and debris (El-Maarry et al. 2016; Pajola et al. 2016a). Therefore, it is likely that this region is more susceptible to mass wasting and cliff collapse leading to exposures of volatile-rich materials. Finally, a couple of outburst locations appear to coincide with the boundary between the Anhur and the Northern hemisphere Aker region (Fig. 7d), which also displays a remarkable morphological dichotomy and sharp scarps with associated talus deposits.

Interestingly, we did not observe outbursts from any of the large fracture systems (e.g. Wosret’s fractured terrains), and only once from a smooth terrain (though notably one of the strongest events, see #16 in Table 1 and Fig. 3). All outburst-related structural features appear in pre-perihelion images, when present (the Wosret pits or the Sobek scarps), and have not been created by the outbursts themselves, but perhaps modified. Over 2016 June–September, *Rosetta* will fly at distances < 10 km from the nucleus, which will allow targeted observations of these areas at very high resolution, and a better understanding of their morphologies.

An important parameter to retrieve when trying to link dust plumes and local morphology is the angle between the plume and the local surface. This can unfortunately not be achieved with the current data set. As explained in Section 2.2, we almost never observed the outburst plumes in more than one image. This means that, although we know quite precisely where the source is, we do not have sufficient information to reconstruct the plume in three dimensions. This is different than for ‘usual’ jets that can be tracked for many hours and fully inverted. Our best current assumption, from visual clues only, is that the flow is perpendicular to the average local surface. However, this assumption may not hold true for the first few metres, especially if the plume arises from a collapsing cliff. Detailed modelling of flow interactions in the vicinity of the sources may help us constraining the angle of release better in future works.

3.4 Local time of outbursts

Knowing the time and location of each outburst, we can calculate the illumination conditions and local time on the comet, in order to understand whether events are more likely to occur under specific temperature conditions. Spacecraft and comet attitudes and trajectories were retrieved with the SPICE library (Acton 1996). The

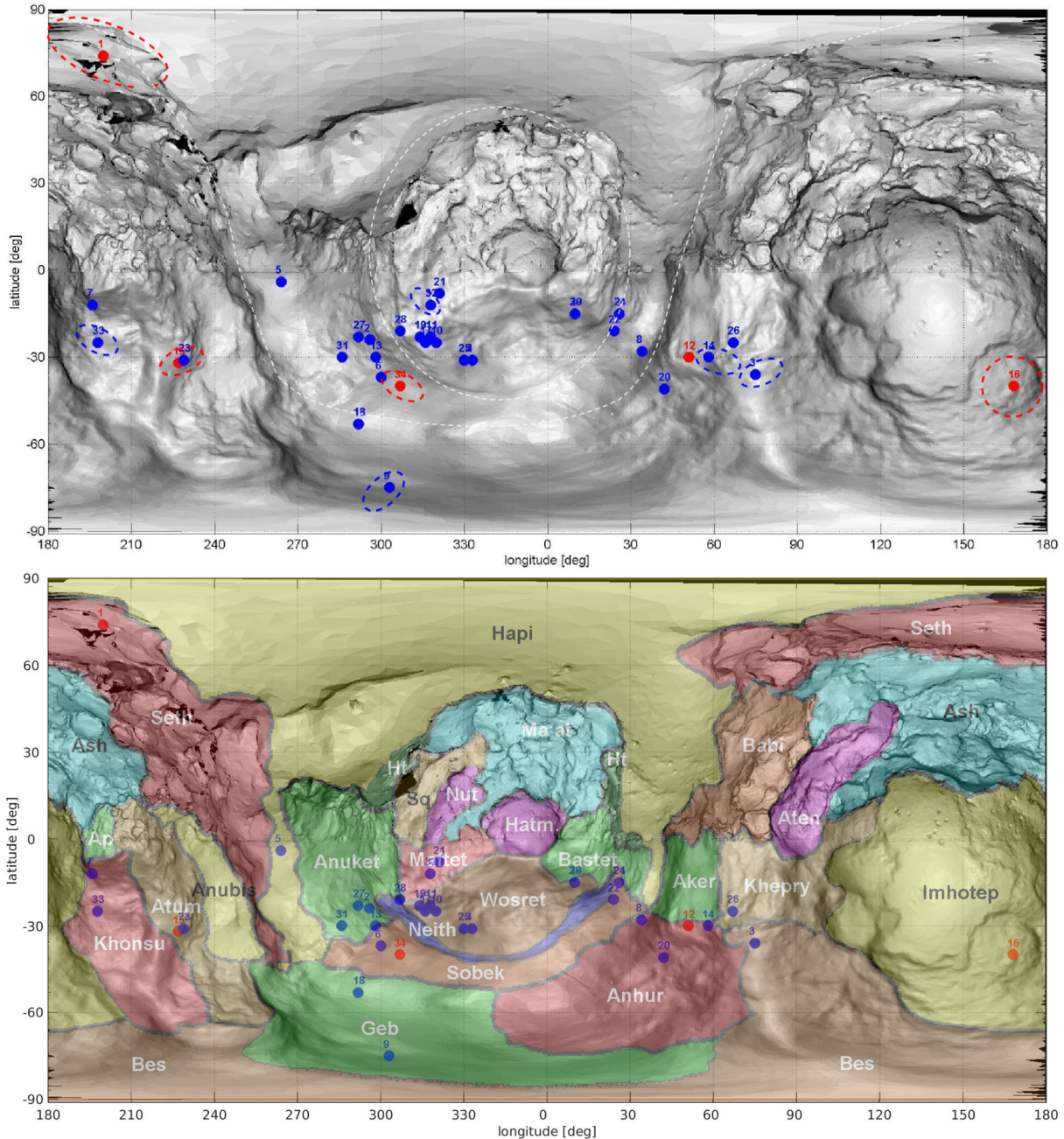


Figure 6. Maps of all summer outbursts detected by the OSIRIS cameras (blue dots) and *Rosetta*'s NavCam (red dots). The top panel plots the sources over a topographic map in which the grey shading represents the local gravitational slope (white: flat, black: vertical wall). Dotted ellipses represent the estimated uncertainty for a few outbursts whose source was not observed directly. Note that this map is a 2D representation of a bi-lobate, strongly concave object, and therefore presents significant distortions. To guide the reader, we indicated with white dashed lines the boundary of the two lobes: the map is centred on the small lobe; the big lobe covers the left–right–bottom edges of the map; and the contact area between the two lobes covers mainly the top of the map (regions Hapi, Neith, Sobek). The three main clusters of outburst sources are located around longitudes 60° (big lobe), 300° (southern neck), and 315° (small lobe), respectively.

local illumination is calculated for the best available shape model of comet 67P: a combination of the model by Preusker et al. (2015) for the Northern hemisphere, and Jorda et al. (2016) for the Southern hemisphere.

Table 1 gives an approximation of the local time since sunrise for each event. This time is calculated from the latitude and longitude offsets between the outburst source and subsolar location, thus not allowing for variations in shadowing due to the topography. We found that 45 per cent of the outbursts occurred after about 3 h of

illumination, i.e. shortly after the local noon. The other 55 per cent of events appear to arise from surfaces that saw their last morning more than 10 h before. If the comet would be a sphere, this would mean night side outbursts. However, due to the very complex shape of 67P, one has to look at these events case by case, and indeed they all seem to arise from a very early local morning, as the Sun just starts to shine on the source area. Fig. 8 shows two examples of local illumination conditions, and illustrates the difficulty in defining the morning terminator.

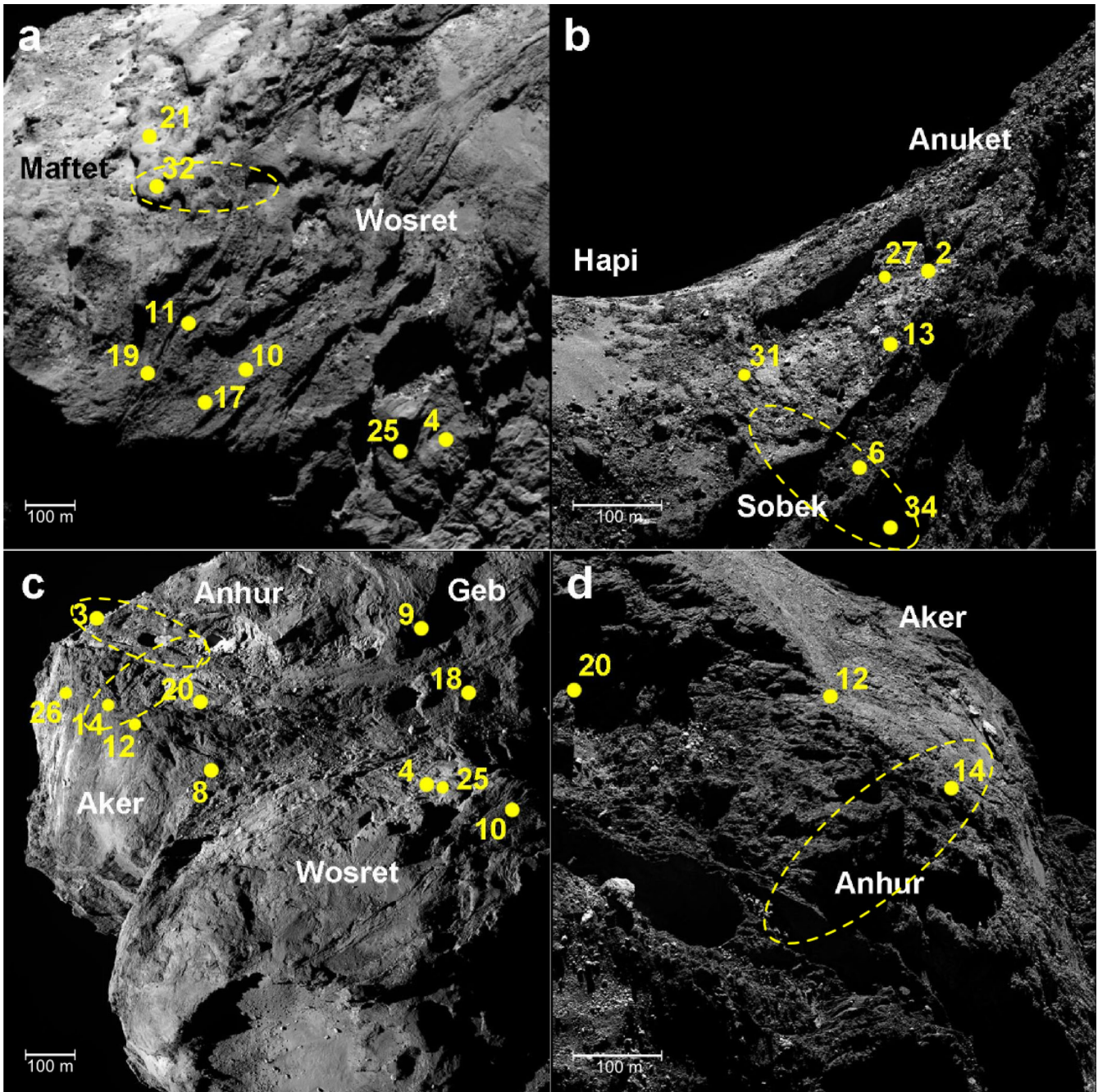


Figure 7. NAC images highlighting morphological and structural settings of a number of candidate outburst locations (numbering consistent with that in Fig. 6 and Table 1) associated with pits and niches in Maftet and Wosret (a), terraced landforms at the boundary between Anuket and Sobek that show extensive debris deposits in the flatter sections (b), the weakly consolidated Anhur region on the large lobe, which shows many niches, alcoves, boulders, and talus deposits (c), and the boundary between Aker and Anhur (d). Images IDs: (a) NAC_2016-01-27T07.44.41.724Z_ID10_1397549800_F22, (b) NAC_2016-05-01T21.52.50.787Z_IDB0_1397549800_F22, (c) NAC_2016-01-23T17.03.47.168Z_IDB0_1397549001_F22, (d) NAC_2016-05-02T07.16.00.860Z_IDB0_1397549900_F22. Images (a) and (c) were acquired from a distance of 76 km (resolution: 1.4 m px⁻¹). Images (b) and (d) were acquired from a distance of 18 km (resolution: 34 cm px⁻¹). Dashed lines indicate the error ellipses for a few sources that could not be well constrained.

There is no correlation between the type of outburst and local time. The dichotomy is more likely related to a different mechanism: (1) noon outbursts may be linked to buried pockets of volatiles, which need time to get heated enough to trigger an outburst. Shortly after noon is when the local surface reaches its maximum temperature. (2) Early morning outbursts, however, occur almost immedi-

ately as the Sun rises. Although the temperature might not yet be too high, the very low thermal inertia ensures that these local times display the steepest temperature gradient. The surface heats up in a few minutes, with a $\Delta T/\Delta t$ (K s⁻¹) large enough to trigger thermal cracking (see for instance Alí-Lagoa, Delbo & Libourel 2015), and can potentially lead to parts of the surface breaking up.

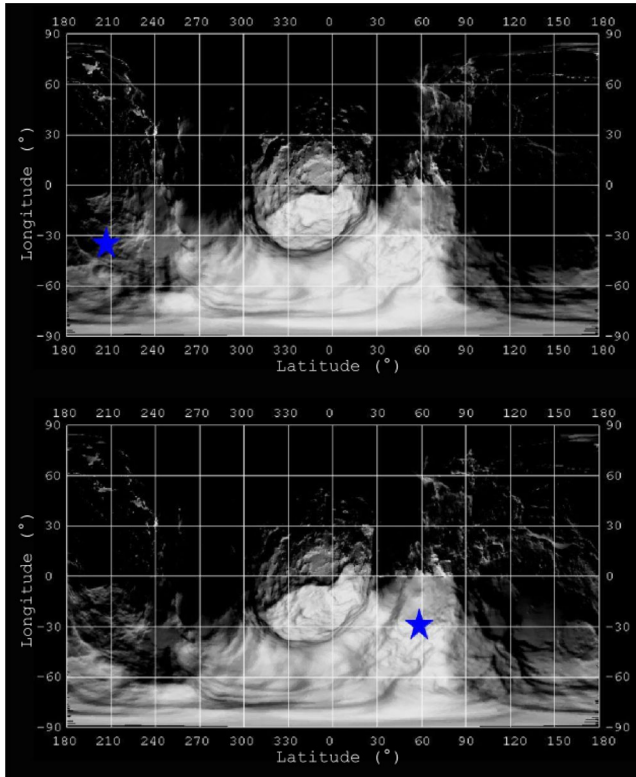


Figure 8. Local illumination conditions for outbursts #7 (top) and #14 (bottom), examples of an early morning and early afternoon events.

Belton et al. (2008) have estimated the local time of 14 mini-outbursts detected on comet 9P/Tempel 1. Like for 67P, they found a non-random distribution. However, they surprisingly never detected dawn or early morning outbursts, which account for more than half of what *Rosetta* observed on 67P. Our current interpretation is that early morning outbursts are a consequence of rapid changes of temperature leading to cracking of the surface. It may not be happening on 9P because the slow rotation (40 h) does not allow high thermal stresses to build up. It may also be that 9P's surface has been more processed than that of 67Ps due to its longer time in the inner Solar system, and the current physical/compositional properties of the upper crust differ on both comets.

4 DISCUSSION: OUTBURSTS MECHANISMS

The name outbursts itself indicate a violent event, akin to an explosion in the subsurface releasing a large amount of material in a very short time relatively to other forms of activity. One of the most prominent theories invokes the build-up of high pressure under the de-volatilized surface layers. The pressure will increase until it overcomes the tensile strength of the surface, at which point the gas pocket will erupt, releasing all the gas and accelerating the surrounding non-volatile material. This will lead to the formation of a small pit or depression (Belton 2013), and potentially expose fresh volatile material that will continue to sublime. Such a mechanism has been discussed for comet 67P in the case of the Imhotep outburst observed in 2015 February (Knollenberg 2016), or the outbursts on 9P/Tempel 1 (Belton et al. 2008; Belton 2013). This process, however, requires that the thermal wave (diurnal or seasonal) is able to reach the depth at which ices are available. Hence, for a region of homogeneous surface properties,

most outbursts should occur around the same local time/local solar incidence. As explained in Section 3.4, we do not see this on 67P; the same area can outburst shortly after noon or early in the morning. It implies that this mechanism requires local compositional or physical heterogeneity on a scale comparable to the outburst footprint (< 100 m), with areas highly enriched in very volatile material such as CO_2 ice or amorphous water ice, the latter being often invoked to explain outbursts detected in ground-based observations (Prialnik & Bar-Nun 1992).

On the basis of our observations of the dust plumes and of the local nucleus morphology, we can infer a possible mechanism generating the outbursts. Vincent et al. (2016) have proposed receding fractured cliffs as the major process responsible for the usual dust jets seen around 67P and other comets. In this scheme, small fractures lead to enhanced inward heat flux and acceleration of the gas in a nozzle-like structure, which form of small jets that can merge into a larger feature as they expand away from the surface. Hoefner (2016) has shown that fractures are an efficient heat trap, but require specific illumination conditions to achieve full potential, namely the Sun shining directly into the fracture so that the maximum input flux reaches the bottom. This means that local activity can only be sustained by having many small fractures subsequently activated as the nucleus rotates. This is indeed the case in many areas, as discussed in Vincent et al. (2016). But what if the solar insolation reaches its maximum over a large fracture? For instance, the crack in the Hapi region that seems to separate the two lobes of the comet (Thomas et al. 2015), or a 500 m long fracture in the Anuket region (El-Maarry et al. 2015a), both a few metres wide? One would expect the same process as for the jets to take place, although enhanced by at least an order of magnitude due to the larger size of those fractures. This high solar input concentrated on a very localized area would lead to an outburst. Unfortunately, although the right illumination conditions are achieved regularly, we have never detected an outburst from a large fracture. This is perhaps not surprising as the heat trap effect would prevent them from retaining much volatile material anyway. The only possibility would be a sudden opening of the fracture either laterally or in depth, which would expose fresh material again.

Here we suggest an alternative, new process, which could explain the observed outbursts without the need for local ice reservoirs, or specific illumination conditions. Jet activity from fractured cliffs leads to a weakening of the wall structure until it collapses, a phenomenon observed on 67P and other comets, and described in detail in Vincent et al. (2016). As most outbursts are located near cliffs presenting evidence of mass wasting, it is tempting to link the two processes. That is to say that with the proposed mechanism, most of the dust is being generated during the collapse, rather than ejected from the surface by an explosion. Of course, we certainly need a gas flow to accelerate the dust away from the surface but the collapse itself may not be triggered by activity. This process requires less energy input than other mechanisms because cometary cliffs are extremely weak (tensile strength < 100 Pa) and any small perturbation can lead to their fall. Additionally, once the dust is released it is easier to accelerate it away because the gas flow does not need to overcome cohesion forces that were keeping the grains on the nucleus surface.

Understanding the details of a cometary cliff collapse is challenging because we do not know much about the mechanical properties of the material. However, it is possible to make a parallel with what happens on Earth. Indeed, as a first approximation, the growth and collapse of cliffs are controlled by the ratio between their inner cohesion and the local gravity (Melosh 2011). This ratio is the same on

Earth and 67P (strength values from Bedjaoui et al. 2010; Groussin 2015; Vincent et al. 2015):

$$\text{Earth: } \frac{c[\text{Pa}]}{g[\text{m s}^{-2}]} = \frac{10^6}{10} = 10^5 \quad [\text{kg m}^{-2}],$$

$$67\text{P: } \frac{c[\text{Pa}]}{g[\text{m s}^{-2}]} = \frac{50}{5.10^{-4}} = 10^5 \quad [\text{kg m}^{-2}].$$

This means that, as a simplified model, one can look at the behaviour of cliff instability on Earth as a proxy for what is taking place on 67P. Upon collapse, terrestrial falling walls like coastal chalk cliffs tend to break not in large chunks, but rather crumble into dust as stresses propagate into an already extremely weak material (Mortimore & Duperret 2004). Note that this is only a qualitative assessment, as Earth cliffs are initially weakened by processes far different than those on the comet, like water erosion at their base or alternating dry weather and heavy rainfall.

The size distribution of material in taluses on 67P shows a consistent lack of large pieces (debris always <10 m; Pajola et al. 2015) which supports a crumbling behaviour rather than a break up in many large fragments. As the wall turns into fine pieces, the dust is immediately available to be picked up by the outward flow of gas that surrounds the nucleus. Moreover, if the cliff happens to be illuminated at that time, the sudden exposure of fresh material on its new wall will increase the local gas flux, further enhancing the outward dust transport, and creating a large fan of dust which we can detect as an outburst.

At least one of our observed outbursts (#1) is a promising candidate for this mechanism. This event was observed by the NavCam on 2015 July 10, and the plume source appears to be close to the Aswan cliff described in Pajola et al. (2016b). The outburst occurred in the middle of the night, in a region receiving only very few insolation because of polar winter (latitude source: +74°, subsolar latitude: −30°). The source region is particularly interesting because it presents some of the most intriguing topographic features of the comet (active pits, see Vincent et al. 2015) and strong evidence for regressive erosion by cliff collapse linked to jet activity (Vincent et al. 2016). In their morphological analysis of the cliffs, Vincent et al. (2016) and Pajola et al. (2016b) have presented large fractures on the edge of the cliff, indicating blocks on the verge of falling. These blocks have now fallen, and the cliff presents a different edge since the second half of 2015 July, along with a modified talus (full details in Pajola et al. 2016, submitted). Based on our observations of this area (very poorly illuminated at that time), we can date the event to sometime in the first half of 2015 July. As we did observe a particularly strong outburst (#1 in Table 1) from this specific place in the right epoch, it seems reasonable to consider a relation between the two events.

On 67P, the typical size of the wall chunks threatening to fall, or having already fallen (see examples in Pajola et al. 2016b; Vincent et al. 2016) is typically a few tens of metres along the edge of the cliff and about 10 m in the other directions. Let us consider a typical wall segment of $50 \times 10 \times 10$ m i.e. 5000 m^3 and $2.35 \times 10^6 \text{ kg}$. We can estimate how much material ends up on the ground upon collapse by looking at the size distribution of blocks in taluses on the nucleus. Pajola et al. (2015) have shown that these blocks are typically smaller than 10 m and their cumulative size distribution follows a power law with a slope between −3.5 and −4. The cumulative size distribution for the Aswan area described above has a power-law slope of −3.9, and the largest boulders are four blocks of about 5 m diameter. By integrating over the size distribution of the talus, and assuming that it is representative of the latest event in this area, we

find that all blocks between 0.5 m (detection limit) and the maximum size of 5 m sum up to a total mass of 4500 m^3 , i.e. 90 per cent of the mass of a typical falling cliff fragment. The remaining 10 per cent are the smaller particles that could be ejected as an outburst plume. Such an event would therefore eject about 500 m^3 of cometary material, or 235 tons. This is perfectly in agreement with our mass estimate for a typical outburst: 60–260 tons; see Section 2.3.

The original perturbation leading to final collapse of a weakened wall remains an open question. Direct activity from the source is an option, but one may also consider vibrations induced by activity in the vicinity or any other process: a small impact, tidal stress, rotation stress, etc. It is difficult, however, to calculate precisely how efficiently vibrations can propagate in the nucleus, as we do not know its internal structure and mechanical properties. We can only get an estimate of the P and S wave velocities using the textbook relations:

$$v_P = \sqrt{\frac{K + (4/3)\mu}{\rho}} \quad \text{and} \quad v_S = \sqrt{\frac{\mu}{\rho}}$$

with K being the bulk modulus, μ the shear modulus, and ρ the material density.

If we take $K \simeq$ compressive strength = 150 Pa, $\mu \simeq$ tensile strength = 50 Pa (Groussin 2015), and $\rho = 470 \text{ kg m}^{-3}$ (Jorda et al. 2016), we obtain $V_P = 0.68 \text{ m s}^{-1}$ and $V_S = 0.33 \text{ m s}^{-1}$.

This velocities are quite low, but comparable to the escape velocity, for instance (0.8 m s^{-1}). We do not know, Q , the coefficient of attenuation of seismic waves for cometary material, but it is likely to be high considering the fact that waves are travelling in a very porous granular material. Therefore, it is reasonable that if cliff collapses are triggered by vibrations, the source must be located in their close vicinity.

We note that Steckloff et al. (2016) have invoked avalanches to explain some of the activity of comet 103P/Hartley 2 and suggested rotational stresses as the trigger. This does not apply to 67P as the outbursts' locations do not correlate with the areas of maximum centrifugal force. Additionally, we observe collapse of consolidated material rather than flows of granular material.

5 CONCLUSION

We have presented a series of 34 transient releases of gas and dust by the nucleus of comet 67P over the 3 months surrounding its perihelion passage in 2015 mid-August.

We found that outbursts occur about every 2.4 nucleus rotations and last at most a few minutes. They are comparable in scale and temporal variation to what has been observed on other comets. The dust plumes released by these events can be classified into three main morphologies: narrow jets, broad plumes, or a combination of both.

We produced a map of the source locations of these events, and discussed the associated local topography. We find that the spatial distribution of outbursts' locations on the nucleus correlates well with morphological region boundaries, especially areas marked by steep scarps or cliffs.

Outbursts occur either in the early morning or shortly after the local noon, possibly indicating two types of processes: morning outbursts may be triggered by thermal stresses linked to the rapid change of temperature, while afternoon events are most likely related to the diurnal or seasonal heat wave reaching volatiles buried deeper in the nucleus than those responsible for the more typical jets. In addition, we propose that some events can be the result of

a completely different mechanism, in which most of the dust is released upon the collapse of a cliff.

This idea will be tested with a more detailed morphological study using forthcoming high-resolution images, joint analysis with other instruments on board *Rosetta*, and numerical modelling.

ACKNOWLEDGEMENTS

OSIRIS was built by a consortium led by the Max Planck Institut für Sonnensystemforschung, Göttingen, Germany; in collaboration with CISAS, University of Padova, Italy; the Laboratoire d'Astrophysique de Marseille, France; the Instituto de Astrofísica de Andalucía, CSIC, Granada, Spain; the Scientific Support Office of the European Space Agency, Noordwijk, the Netherlands; the Instituto Nacional de Técnica Aeroespacial, Madrid, Spain; the Universidad Politécnica de Madrid, Spain; the Department of Physics and Astronomy of Uppsala University, Sweden; and the Institut für Datentechnik und Kommunikationsnetze der Technischen Universität Braunschweig, Germany.

The support of the national funding agencies of Germany (DLR), France (CNES), Italy (ASI), Spain (MINECO), Sweden (SNSB), and the ESA Technical Directorate is gratefully acknowledged.

We thank the *Rosetta* Science Ground Segment at ESAC, the *Rosetta* Mission Operations Centre at ESOC and the *Rosetta* Project at ESTEC for their outstanding work enabling the science return of the *Rosetta* Mission.

All *Rosetta* NavCam images are released under the Creative Commons license ESA/*Rosetta*/NAVCAM - CC BY-SA IGO 3.0. This research has made use of NASA's Astrophysics Data System Bibliographic Services.

The authors wish to thank M. J. S. Belton for his helpful criticism of the paper during the review process.

REFERENCES

- A'Hearn M. F. et al., 2005, *Science*, 310, 258
 Acton C. H., 1996, *Planet. Space Sci.*, 44, 65
 Alf-Lagoa V., Delbo M., Libourel G., 2015, *ApJ*, 810, L22
 Bedjaoui M., Allal M., Duperré A., Taibi A., Rivoalen E., 2010, *Jordan J. Civ. Eng.*, 4, 63
 Belton M. J. S., 2013, *Icarus*, 222, 477
 Belton M. J. S., Feldman P. D., A'Hearn M. F., Carcich B., 2008, *Icarus*, 198, 189
 El-Maarry M. R. et al., 2015a, *Geophys. Res. Lett.*, 42, 5170
 El-Maarry M. R. et al., 2015b, *A&A*, 583, A26
 El-Maarry M. R. et al., 2016, *A&A*, 593, A110
 Fulle M. et al., 2016, *ApJ*, 821, 19
 Groussin O. et al., 2015, *A&A*, 583, A32
 Hoefner S. et al., 2016, *A&A*, in press
 Ip W. H. et al., 2016, *EGU proceedings*
 Jorda L. et al., 2016, *Icarus*, 277, 257
 Knollenberg J. et al., 2016, *A&A*, in press
 Lara L. M. et al., 2015, *A&A*, 583, A9
 Lin Z.-Y. et al., 2015, *A&A*, 583, A11
 Lin Z.-Y. et al., 2016, *A&A*, 588, L3
 Melosh H. J., 2011, *Planetary Surface Processes*. Cambridge Univ. Press, Cambridge
 Mortimore R. N., Duperré A., 2004, *Coastal Chalk Cliff Instability*. Geological Society of London
 Pajola M. et al., 2015, *A&A*, 583, A37
 Pajola M. et al., 2016a, *A&A*, 592, L2
 Pajola M. et al., 2016b, *A&A*, 592, A69
 Preusker F. et al., 2015, *A&A*, 583, A33
 Prialnik D., Bar-Nun A., 1992, *A&A*, 258, L9
 Steckloff J. K., Graves K., Hirabayashi M., Melosh H. J., Richardson J. E., 2016, *Icarus*, 272, 60
 Thomas N. et al., 2015, *Science*, 347, 6220
 Tubiana C. et al., 2015, *A&A*, 573, A62
 Vincent J.-B. et al., 2015, *Nature*, 523, 63
 Vincent J.-B. et al., 2016, *A&A*, 587, A14
- ¹Max-Planck Institut für Sonnensystemforschung, Justus-von-Liebig-Weg 3, D-37077 Göttingen, Germany
²Department for Astronomy, University of Maryland, College Park, MD 20742-2421, USA
³Institute of Astronomy, National Central University, 32054 Chung-Li, Taiwan
⁴Physikalisches Institut, Sidlerstrasse 5, University of Bern, CH-3012 Bern, Switzerland
⁵NASA Ames Research Center, Moffett Field, CA 94035, USA
⁶Centro di Ateneo di Studi ed Attività Spaziali 'Giuseppe Colombo' (CISAS), University of Padova, Via Venezia 15, I-35131 Padova, Italy
⁷Department of Physics and Astronomy 'G. Galilei', University of Padova, Vic. Osservatorio 3, I-35122 Padova, Italy
⁸Aix Marseille Université, CNRS, LAM (Laboratoire d'Astrophysique de Marseille) UMR 7326, F-13388 Marseille, France
⁹Centro de Astrobiología (INTA-CSIC), European Space Agency (ESA), European Space Astronomy Centre (ESAC), PO Box 78, E-28691 Villanueva de la Canada, Madrid, Spain
¹⁰International Space Science Institute, Hallerstrasse 6, CH-3012 Bern, Switzerland
¹¹Scientific Support Office, European Space Agency, NL-2201 Noordwijk, the Netherlands
¹²PAS Space Research Center, Bartycka 18A, PL-00716 Warszawa, Poland
¹³Department of Physics and Astronomy, Uppsala University, Box 516, SE-75120 Uppsala, Sweden
¹⁴Institute for Geophysics and Extraterrestrial Physics, TU Braunschweig, D-38106 Braunschweig, Germany
¹⁵LESIA, Observatoire de Paris, CNRS, UPMC Univ Paris 06, Univ. Paris-Diderot, 5 Place J. Janssen, F-92195 Meudon Principal Cedex, France
¹⁶LATMOS, CNRS/UVSQ/IPSL, 11 Boulevard d'Alembert, F-78280 Guyancourt, France
¹⁷ESA/ESAC, Camino Bajo del Castillo s/n, Ur. Villafranca del Castillo, E-28692 Villanueva de la Canada, Madrid, Spain
¹⁸INAF Osservatorio Astronomico di Padova, Vicolo dell'Osservatorio 5, I-35122 Padova, Italy
¹⁹CNR-IFN UOS Padova LUXOR, Via Trasea 7, I-35131 Padova, Italy
²⁰NASA Jet Propulsion Laboratory, 4800 Oak Grove Drive, Pasadena, CA 91109, USA
²¹Department of Industrial Engineering University of Padova Via Venezia, 1, I-35131 Padova, Italy
²²University of Trento, via Sommarive, 9, I-38123 Trento, Italy
²³INAF - Osservatorio Astronomico di Trieste, via Tiepolo 11, I-34143 Trieste, Italy
²⁴Instituto de Astrofísica de Andalucía-CSIC, Glorieta de la Astronomía, E-18008 Granada, Spain
²⁵Institute of Planetary Research, DLR, Rutherfordstrasse 2, D-12489 Berlin, Germany
²⁶Space Science Institute, Macau University of Science and Technology, Macau
²⁷Budapest University of Technology and Economics, Department of Mechatronics, Optics and Engineering Informatics, Muegyetem rkp 3, Budapest, Hungary
²⁸Dipartimento di Geoscienze, University of Padova, via Granedigo 6, I-35131 Padova, Italy
²⁹Department of Information Engineering, University of Padova, Via Gradenigo 6/B, I-35131 Padova, Italy
³⁰Observatory of the Hungarian Academy of Sciences, PO Box 67, 1525 Budapest, Hungary

This paper has been typeset from a $\text{\TeX}/\text{\LaTeX}$ file prepared by the author.